# Influence of an atomic resonance on the coherent control of the photoionization process

```
E. V. Gryzlova, P. Carpeggiani, 1,* M. M. Popova, M. D. Kiselev, N. Douguet, M. Reduzzi, M. Negro, A. Comby, 1,†
 H. Ahmadi, V. Wanie, 1,4,± M. C. Castrovilli, A. Fischer, P. Eng-Johnsson, M. Meyer, K. Bartschat, S. M. Burkov,
T. Csizmadia, M. Dumergue, S. Kühn, N. G. Harshitha, M. Fule, F. Aeenehvand, F. Stienkemeier, D. Iablonskyi, 11
 K. Ueda, <sup>11</sup> P. Finetti, <sup>12</sup> M. Zangrando, <sup>12,13</sup> N. Mahne, <sup>13</sup> K. L. Ishikawa, <sup>14,15,16</sup> O. Plekan, <sup>12</sup> K. C. Prince, <sup>12</sup> E. Allaria, <sup>12</sup> L. Giannessi, <sup>12</sup> C. Callegari, <sup>12</sup> A. N. Grum-Grzhimailo, and G. Sansone <sup>10</sup>
                                            <sup>1</sup>Dipartimento di Fisica Politecnico, Milano 20129, Italy
                            <sup>2</sup>Department of Physics, Kennesaw State University, Kennesaw, Georgia 30144, USA
                         <sup>3</sup>Department of Physics and Astronomy, Drake University, Des Moines, Iowa 50311, USA
                      <sup>4</sup>Centre Énergie Matériaux Télécommunications, Institut National de la Recherche Scientifique,
                                                       Varennes, Québec, Canada J3X 1S2
                       <sup>5</sup>Consiglio Nazionale delle Ricerche-Istituto Fotonica e Nanotecnologie, Milano 20129, Italy
                                   <sup>6</sup>Max-Planck Institute for Nuclear Physics, Heidelberg 69117, Germany
                                      <sup>7</sup>Department of Physics, Lund University, Lund SE-221 00, Sweden
                                                 <sup>8</sup>European XFEL, Schenefeld 22869, Germany
                                        <sup>9</sup>ELI ALPS, ELI-HU Non-Profit Ltd., H-6728 Szeged, Hungary
                        <sup>10</sup>Physikalisches Institut der Albert-Ludwigs-Universität Freiburg, Freiburg 79014, Germany
              <sup>11</sup>Institute of Multidisciplinary Research for Advanced Materials, Tohoku University, Sendai 980-8577, Japan
                                              <sup>12</sup>Elettra-Sincrotrone Trieste, Basovizza 34149, Italy
                                                       <sup>13</sup>IOM-CNR, Basovizza 34149, Italy
           <sup>14</sup>Department of Nuclear Engineering and Management, Graduate School of Engineering, The University of Tokyo,
                                                7-3-1 Hongo, Bunkyo-ku, Tokyo 113-8656, Japan
                             <sup>15</sup>Photon Science Center, Graduate School of Engineering, The University of Tokyo,
                                                7-3-1 Hongo, Bunkyo-ku, Tokyo 113-8656, Japan
                          <sup>16</sup>Research Institute for Photon Science and Laser Technology, The University of Tokyo,
                                               7-3-1 Hongo, Bunkyo-ku, Tokyo 113-0033, Japan
```



(Received 25 July 2021; revised 1 August 2022; accepted 5 August 2022; published 23 September 2022)

In coherent control schemes, pathways connecting an initial and a final state can be independently controlled by manipulating the complex amplitudes of their transition matrix elements. For paths characterized by the absorption of multiple photons, these quantities depend on the magnitude and phase between the intermediate steps, and are expected to be strongly affected by the presence of resonances. We investigate the coherent control of the photoemission process in neon using a phase-controlled two-color extreme ultraviolet pulse with frequency in proximity of an excited energy state. Using helium as a reference, we show that the presence of such a resonance in neon modifies the amplitude and phase of the asymmetric emission of photoelectrons. Theoretical simulations based on perturbation theory are in fair agreement with the experimental observations.

DOI: 10.1103/PhysRevResearch.4.033231

## I. INTRODUCTION

Coherent control is a fundamental quantum strategy for steering the outcome of a chemical reaction or a physical

Published by the American Physical Society under the terms of the Creative Commons Attribution 4.0 International license. Further distribution of this work must maintain attribution to the author(s) and the published article's title, journal citation, and DOI.

process. This control relies on the premise that several quantum-mechanical paths can connect the initial and final states of a system, with each of them being characterized by a complex transition matrix element. The interference of these complex terms governs the properties of the final state, which can be controlled by manipulating the contributions associated with one or more pathways. As described in [1], coherent control schemes are widely applied in numerous fields, such as chemical reactions [2,3], biological processes [4], ultracold physics [5], quantum information [6], and attosecond physics [7].

Typically, coherent control is implemented by shaping, in both amplitude and phase, the spectral components of the laser pulses that interact with the quantum system [8]. For nonlinear pathways characterized by the absorption of several photons, the structure of the intermediate energy levels of

<sup>\*</sup>Present address: Technische Universität Wien 1040, Austria.

<sup>&</sup>lt;sup>†</sup>Present address: Université de Bordeaux-CNRS-CEA, CELIA, UMR5107, F33405 Talence, France.

<sup>&</sup>lt;sup>‡</sup>Present address: Center for Free-Electron Laser Science CFEL, Deutsches Elektronen-Synchrotron DESY, 22607 Hamburg, Germany.

the system is expected to play a fundamental role and to significantly affect the overall complex amplitude of the path. The presence of an intermediate resonance, together with the control of the energy of the interacting laser pulse, offers an additional degree of freedom for controlling the final outcome of the reaction. Even though such controls are widely used in coherent schemes in the visible range [9–12], the effect of an intermediate energy resonance on the characteristics of the final state has not yet been observed in experiments in the extreme ultraviolet (XUV) range. However, recent theoretical works suggest that resonances in the nonlinear pathway leading to photoemission should influence the photoelectron angular distributions (PADs) as a function of the photon energy [13–15].

In the XUV spectral range, pulse shaping is extremely challenging, due to the lack of suitable materials and flexible schemes for controlling the amplitude and phase of the pulses. An alternative approach, based on the manipulation of the electron bunch generating the XUV pulses, instead of the XUV spectrum itself, was recently demonstrated at the seeded free-electron laser (FEL) FERMI [16]. Using this approach, phase differences corresponding to delays as small as 3 attoseconds (as) (1 as =  $10^{-18}$  s) between two harmonics of the seed laser [17] and complete pulse shaping of a multicolor XUV spectrum [18–20] were demonstrated.

In the present work, we investigate the effect of an atomic resonance on the coherent control of the photoionization process in neon by using a two-color, tunable XUV pulse, composed of a fundamental frequency  $(\omega)$  and its second harmonic  $(2\omega)$ . The energy of the fundamental was tuned around the  $2p \rightarrow 4s$  atomic resonance in neon  $(\hbar\omega \approx 19.75 \text{ eV})$ , and the PADs were characterized by a velocity map imaging (VMI) spectrometer [21].

The effect of the intermediate resonance on the pathway characterized by the absorption of two photons of the fundamental pulse [blue lines in Fig. 1(a)] is qualitatively presented in Fig. 1(b) using the classical Lorentz model for the light-matter interaction. The presence of the resonance around 19.75 eV strongly affects the magnitude and phase of the transition dipole moment between the ground and the excited state as a function of the photon energy  $\hbar\omega$ . This variation is expected to be imprinted in the overall magnitude  $(d_1)$  and phase  $(\varphi_1)$  of the nonlinear pathway, which also includes the contribution of the nonresonant two-photon ionization [light-blue lines in Fig. 1(a)], connecting the initial and final states. In contrast, due to the absence of resonances in the continuum, the magnitude  $(d_2)$  and phase  $(\varphi_2)$  of the linear pathway [purple lines in Fig. 1(a)] should present only a negligible variation when the photon energy is changed.

The photoelectron signal generated by the two-color field can be described by the relation

$$S(\mathbf{p},\tau) = \left| E_1^2 e^{i2\psi_1} d_1(\mathbf{p}) e^{i\varphi_1(\mathbf{p})} + E_2 e^{i(\psi_2 - 2\omega\tau)} d_2(\mathbf{p}) e^{i\varphi_2(\mathbf{p})} \right|^2,$$
(1)

where  $E_1$ ,  $E_2$ ,  $\psi_1$ , and  $\psi_2$  denote the (real) magnitudes and phases of the fundamental and the second harmonic delayed by  $\tau$ , respectively. The terms  $d_i(\mathbf{p})$  and  $\varphi_i(\mathbf{p})$  depend on the momentum  $\mathbf{p}$  of the photoelectron and indicate the magnitude and phase of the total dipole matrix element for the nonlinear (i=1) and linear (i=2) processes, respectively.

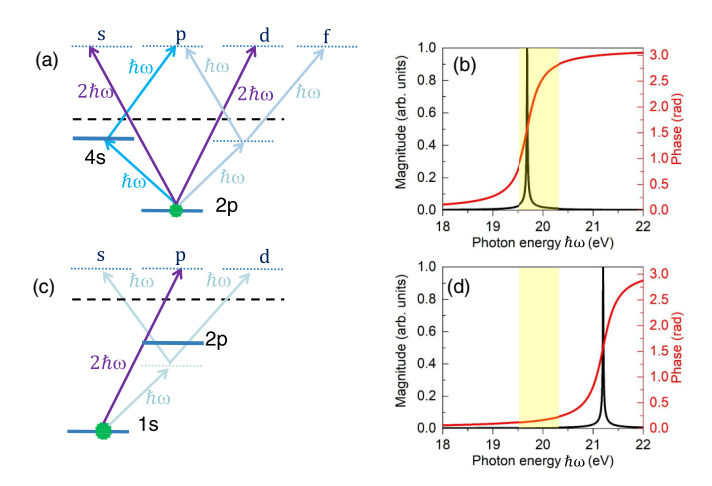


FIG. 1. Coherent control of photoionization in neon (a), (b) and helium (c), (d). A photoelectron can be emitted via two different pathways, characterized by the absorption of two photons of the fundamental  $\omega$  (resonant, blue lines; nonresonant, light-blue lines) or one photon of the second harmonic  $2\omega$  (purple lines). The position of the 4s resonance in neon (a) and that of the 2p in helium (c) are indicated. The dashed lines indicate the ionization threshold. The magnitude (black) and phase (red) of the dipole matrix element using the classical Lorentz model are shown for neon in (b) and helium in (d). The shaded yellow area indicates the photon energy range investigated in the present work.

Photoionization paths characterized by the absorption of two photons of the fundamental or by a single photon of the second harmonic lead to final states in the continuum characterized by different parities [see Fig. 1(a)]. The coherent sum of these two contributions results in the asymmetric emission of photoelectrons along the polarization direction of the XUV pulses. Taking advantage of this property, we characterize the influence of the intermediate resonance by monitoring the characteristics of the asymmetric PADs as a function of the fundamental photon energy.

In the experiment, however, upon changing the fundamental photon energy, an additional, unknown relative phase between the two colors or a modification of the ratio of their amplitudes can be introduced (see Sec. II).

In order to isolate the effect of the resonance on the coherent control mechanism, the experiment was performed in a mixture of neon and helium atoms, using the signal derived from the photoelectrons ejected from the latter target as a reference (see Sec. IV). Since the photon energy around the  $2p \rightarrow 4s$  resonance in neon is sufficiently distant from all dipole-allowed resonances in helium [see Fig. 1(c)], neither the magnitude nor the phase of the nonlinear pathways are expected to change significantly in helium [22]. The first dipole-allowed resonance (1s  $\rightarrow$  2p at 21.2 eV) is sufficiently far away in energy to introduce only a negligible variation in magnitude and phase of the transition matrix dipole moment for small variations of the photon energy around 19.75 eV, as schematically shown in Fig. 1(d). This qualitative conclusion is also supported by simulations based on solving the two-electron time-dependent Schrödinger equation (TDSE) [23–25] (see Sec. III).

This paper is organized as follows: In Sec. II we present the experimental setup and introduce the asymmetry parameter

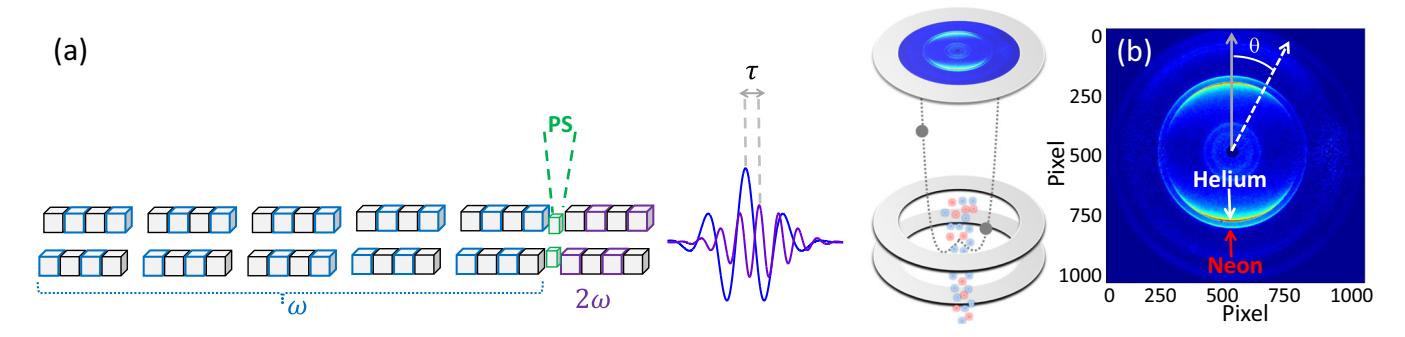


FIG. 2. (a) Experimental setup. Schematic view of the six undulators available at FERMI. The phase shifter PS placed between the fifth and sixth undulator was used to change the relative phase  $2\omega\tau$  between the two colors. The gas jet was composed of a mixture of neon and helium (shown with red and blue circles). (b) VMI spectrum (noninverted and background corrected) showing the angular-resolved photoelectron spectra emitted by the two-color fields in a mixture of neon and helium. The inner and outer rings correspond to the photoelectrons generated in helium (white) and neon (red), respectively. The gray line indicates the polarization direction of the FEL pulse. The angle  $\theta$  defines the emission direction of the photoelectrons.

measured in the experiment. Section III describes the theoretical models used to simulate the photoelectron spectra obtained in helium and neon. The comparison of the experimental and theoretical data is presented in Sec. IV. The conclusions and future perspectives are discussed in Sec. V.

## II. EXPERIMENTAL SETUP

The experiment (see Fig. 2) was performed at the seeded FEL FERMI [16] at the low-density-matter beamline [26]. The two-color XUV pulse was generated by tuning the first five undulators at the fundamental frequency  $\omega$  (between 19.60 and 20.20 eV) and the last undulator at its second harmonic  $2\omega$  (between 39.20 and 40.40 eV).

The duration of the XUV pulses was estimated to be about 60 fs [27] (full width at half maximum). The XUV field was focused using a Kirkpatrick-Baez arrangement (not shown in Fig. 2) in the focal position of the VMI spectrometer. Considering the energy of the fundamental measured using a gas monitor placed after the undulators ( $E=33~\mu\mathrm{J}$ ; not shown), we estimated a peak intensity of  $I_1\approx 10^{13}~\mathrm{W/cm^2}$  for the fundamental frequency. The intensity of the second harmonic was estimated as  $I_2\approx 2\times 10^{12}~\mathrm{W/cm^2}$ .

The photon beam was crossed with a cold atomic jet composed of a mixture of helium and neon. The percentage of the mixture was optimized considering the cross sections to obtain comparable photoelectron signals for the two gases.

A phase shifter placed between the fifth and sixth undulator delayed the electron bunch with respect to the field generated in the first undulators [28]. For each delay, 3000 consecutive shots were acquired. The images were inverted using an onion-peeling algorithm [29,30], which reduces the influence of experimental noise on the reconstructed photoelectron distribution [31]. The intensities of the photoelectron spectra were integrated over opposite hemispheres. At each photon energy of the fundamental, the relative delay  $\tau$  between the two fields was changed in steps of  $\Delta \tau = 13.2$  as up to  $\tau_{\rm max} = 210$  as, corresponding to twice the period of the second harmonic  $(2\omega\tau_{\rm max} = 4\pi)$ . The best resolution achievable with this delay line was estimated to be about 3 as [17].

The evolution of the asymmetry as a function of the delay  $\tau$  is then expected to oscillate according to the expression

$$A^{(k)}(\omega,\tau) = A_{\omega}^{(k)} \cos\left(2\omega\tau - \phi_{\omega}^{(k)}\right) \tag{2}$$

as a function of  $\tau$ . The superscript (k) is used to distinguish between neon (k = n) and helium (k = h).

Figure 2(b) presents a typical photoelectron spectrum acquired in the gas mixture using the VMI spectrometer. Fits were performed to extract the respective amplitudes and phases of the oscillations.

The asymmetry for photoelectrons emitted from neon and helium was estimated as

$$A^{(k)}(\omega,\tau) = \frac{W_u^{(k)}(\omega,\tau) - W_d^{(k)}(\omega,\tau)}{W_u^{(k)}(\omega,\tau) + W_d^{(k)}(\omega,\tau)},\tag{3}$$

where  $W_u^{(k)}$  and  $W_d^{(k)}$  indicate the photoelectron signal integrated over the corresponding peak, emitted in the upward  $(0 < \theta < \pi/2)$  and downward  $(\pi/2 < \theta < \pi)$  hemispheres with respect to the polarization direction of the XUV field [cf. Fig. 2(b)]. The error bars for the asymmetry parameters were determined by dividing the data into five subsets. Then the standard deviation was calculated for the entire dataset.

However, the change of fundamental photon energy of the FEL pulse can introduce an additional, unknown relative phase between the two frequencies and also a variation of the ratio of the amplitudes. Indeed, the delay depends on the superposition of the magnetic fields of the phase shifter and the undulators. While the phase shifter field is known, the second contribution is known only when the two undulators are set to the same resonance wavelength (i.e., the same undulator gap), but not different ones. As a result, a change in photon energy (which in the case of FERMI corresponds to a change of the undulator gap), can introduce an additional phase shift and a variation of the intensity ratio between the two colors, which is not known a priori. In order to compensate for these variations, the experiment was performed in a neon/helium mixture, using the amplitude and phase of the asymmetries measured in helium as reference.

#### III. THEORETICAL DESCRIPTION

Calculations for neon were performed in the lowest nonvanishing order of nonstationary perturbation theory (PT) with multiconfiguration intermediate-coupling atomic wave functions [32].

We consider the PAD in the electric dipole (E1) approximation for two linearly polarized beams with collinear electric field vectors. The field is described by the relation

$$E(t) = \epsilon F(t) [E_1 \cos(\omega t + \psi_1) + E_2 \cos(2\omega t + \psi_2 - 2\omega \tau)]. \tag{4}$$

Here  $\epsilon$  is the unit polarization vector along the z axis,  $\psi_{1,2}$  are the phases of the harmonics, and F(t) is the pulse envelope containing N optical cycles. We used  $F(t) = \sin^2 \frac{\omega t}{2N}$  for  $0 \leqslant t \leqslant \frac{2\pi}{\omega} N$  and 0 otherwise. The field amplitude in

atomic units is  $E_{1,2} = 0.5338 \times 10^{-8} \sqrt{I_{1,2}}$  with I denoting the peak intensity in W/cm<sup>2</sup>. We took N = 500, which corresponds to a total pulse duration (beginning to end) of  $\approx 100$  fs or  $\approx 40$  fs FWHM of the intensity.

Performing transformations similar to those described in [32,33], we obtain the angle-differential PAD for the solid-angle  $d\Omega$  as a sum of three terms:

$$\frac{dW}{d\Omega} = \frac{dW}{d\Omega}^{(I)} + \frac{dW}{d\Omega}^{(II)} + \frac{dW}{d\Omega}^{(III)}.$$
 (5)

The first and second terms are the PADs due to one-photon ionization by the second harmonic and two-photon ionization by the fundamental frequency, respectively. The third term is due to the interference between the two paths. The three components are given in terms of Legendre polynomials as

$$\frac{dW}{d\Omega}^{(1)} = \frac{1}{4\pi} \sum_{kll'KK'} \hat{l} \hat{l}' \hat{K} \hat{K}' (-1)^{J_f - 1/2} (10, 10 | k0) (l0, l'0 | k0) 
\times \begin{cases} k & 1 & 1 \\ \frac{1}{2} & K' & K \end{cases} \begin{cases} k & l & l' \\ J_f & K' & K \end{cases} D^{(1)} (J_f l[K]_1) [D^{(1)} (J_f l'[K']_1)]^* P_k(\cos \vartheta), \tag{6}$$

$$\frac{dW}{d\Omega}^{(II)} = \frac{1}{12\pi} \sum_{kll'KK'JJ'} \hat{l} \hat{l}' \hat{K} \hat{K}' (-1)^{J_f - 1/2} (J0, J'0 | k0) (l0, l'0 | k0)$$

$$\times \begin{cases} k & J & J' \\ \frac{1}{2} & K' & K \end{cases} \begin{cases} k & l & l' \\ J_f & K' & K \end{cases} D^{(2)} (J_f l[K]_J) [D^{(2)} (J_f l'[K']_{J'})]^* P_k(\cos \vartheta), \tag{7}$$

$$\frac{dW}{d\Omega}^{(III)} = \frac{1}{2\sqrt{3\pi}} \sum_{kll'KK'J'} \hat{l} \hat{l}' \hat{K} \hat{K}' (-1)^{J_f - 1/2} (10, J'0 | k0) (l0, l'0 | k0)$$

$$\times \begin{cases} k & 1 & J' \\ \frac{1}{2} & K' & K \end{cases} \begin{cases} k & l & l' \\ J_f & K' & K \end{cases} Re \{ D^{(1)} (J_f l[K]_1) [D^{(2)} (J_f l'[K']_{J'})]^* \} P_k(\cos \vartheta), \tag{8}$$

where  $\theta$  is counted from the direction of the electric field. In Eqs. (6)–(8) we use the jK-coupling scheme, where the total angular momentum  $J_f$  of the residual ion is first coupled to the orbital angular momentum of the photoelectron l,  $J_f + l = K$ , with subsequent coupling to the spin of this electron, K + s = J. Standard notations for the Wigner 6j symbols and Clebsch-Gordan coefficients are used, and we abbreviated  $\hat{a} = \sqrt{2a+1}$ . We also introduced shorthand notations for the first-order and second-order partial-wave transition amplitudes in terms of the reduced dipole matrix elements:

$$D^{(1)}(J_f l[K]_1) \equiv -i^{-l} e^{i\delta_l} T^{(1)} \langle J_f l[K] : 1^- || D || 0^+ \rangle, \tag{9}$$

$$D^{(2)}(J_f l[K]_J) \equiv -i^{-l} e^{i\delta_l}(10, 10 \mid J0) \left( \sum_n T_{\varepsilon_n}^{(2)} \langle J_f l[K] : J^+ \mid \mid D \mid \mid \xi_n : 1^- \rangle \langle \xi_n : 1^- \mid \mid D \mid \mid 0^+ \rangle \right), \tag{10}$$

where  $\delta_l$  is the scattering phase in the photoionization channel with orbital angular momentum l. The summation in (10) proceeds over all intermediate states, and the time-dependent factors are

$$T^{(1)} = \frac{E_2}{2} e^{-i\psi_2 + 2i\omega\tau} \int_0^{NT} F(t') e^{i(\varepsilon - \varepsilon_0 - 2\omega t')} dt', \quad (11)$$

$$T_{\varepsilon_n}^{(2)} = e^{-i\psi_1} \frac{E_1^2}{4} \int_0^{NT} F(t') e^{i(\varepsilon - \varepsilon_n - \omega)t'}$$

$$\times \int_0^{t'} F(t'') e^{i(\varepsilon_n - \varepsilon_0 - \omega)t''} dt'' dt', \quad (12)$$

where  $\varepsilon$  is the energy of the photoelectron,  $\varepsilon_0$  is the energy of the initial state, and  $\varepsilon_n$  is the energy of an intermediate state.

### A. Applicability of perturbation theory

The question may arise whether PT is applicable at intensities up to  $I_1 = 10^{13}$  W/cm<sup>2</sup>. To check this point, we solved the TDSE in the single-active electron (SAE) approximation for an electron initially in the 2p orbital of the neon ground state, employing the same basic method and the associated computer code described by Pauly *et al.* [34]. We used the same potential as in previous investigations [32], in which we calculated the 2p and other bound orbitals such as 4s and 3d, as well as the continuum orbitals, to represent the ejected electron. The above potential produces the first ionization potential of neon, i.e., the binding energy of the 2p electron, very well. The calculations were carried out in the length gauge of the electric dipole operator. Tests carried out by varying

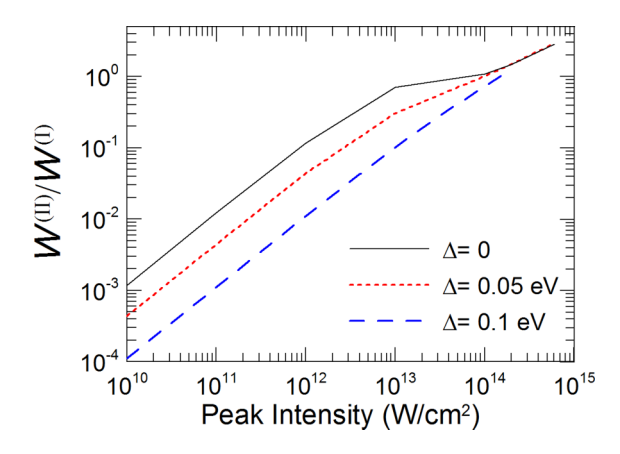


FIG. 3. Ratio of ionization probability by the second harmonic and the fundamental for different detunings  $\Delta$  (0 eV: solid, black line; 0.05 eV: red, dotted line; 0.1 eV: blue, dashed line), as calculated using the TDSE model.

the time step, the radial grid, and the number of partial waves give us confidence that any inaccuracies in the predictions are due to the inherent limitations of the SAE model rather than numerical issues.

Simulations were performed for different intensities of the fundamental frequency and for different detunings  $\Delta$  between the fundamental photon energies and the resonance energy of the  $2p \to 4s$  transition. The results are shown in Fig. 3 for the resonant case ( $\Delta=0\,\mathrm{eV}$ ) and for photon energies close to the resonance ( $\Delta=0.05$  and 0.1 eV). Saturation effects start playing a role only for intensities higher than  $10^{13}\,\mathrm{W/cm^2}$  and exactly in resonance (black curve), thus indicating the validity of the predictions of the PT approach for our conditions.

### B. Atomic model

The photon energy interval investigated in the experiment is dominated by five excited states of neon, which, in the jK-coupling scheme, are  $[2p^5]4s[\frac{3}{2}]_1$  (19.688 eV),  $4s'[\frac{1}{2}]_1$  (19.780 eV),  $3d[\frac{1}{2}]_1$  (20.025 eV),  $3d[\frac{3}{2}]_1$  (20.040 eV), and  $3d'[\frac{3}{2}]_1$  (20.139 eV). These levels are coupled to the ground state by electric dipole transitions. Strong mixing between the 4s and 4s' states and the presence of the 3d states in their

vicinity distinguishes our case from previous theoretical studies of coherent control in  $\omega + 2\omega$  ionization with intermediate resonances [13–15]. The experimental excitation energies of the five states were imposed.

The ground state of neon was obtained by a fully self-consistent calculation of the  $1s^22s^22p^6$  configuration. To obtain the multiconfiguration wave functions of the intermediate excited states  $|\xi_n:1^-\rangle$  with total electronic angular momentum J=1 and odd parity, we performed separate self-consistent calculations for each of the basis configurations  $1s^22s^22p^53s$ ,  $1s^22s^22p^54s$ ,  $1s^22s^22p^55s$ ,  $1s^22s^22p^56s$ ,  $1s^22s^22p^53d$ ,  $1s^22s^22p^53d$ ,  $1s^22s^22p^53d$ ,  $1s^22s^22p^53d$ ,  $1s^22s^22p^53d$  with  $J^\pi=1^-$  for all possible terms in the LS-coupling scheme, with subsequent diagonalization of the Breit-Pauli Hamiltonian for the  $J^\pi=1^-$  states. We fully accounted for the nonorthogonality of the one-electron orbitals using the B-spline R-matrix code of Zatsarinny [35]. The wave functions of the intermediate states in Eq. (10) are thus expanded as

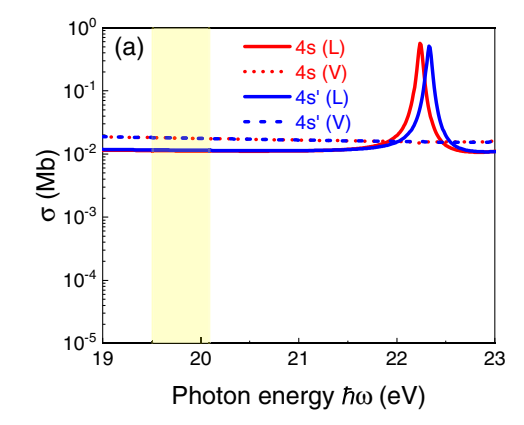
$$|\xi_n:1^-\rangle = \sum_p \alpha_p^n |\chi_p L_p S_p:1^-\rangle, \tag{13}$$

where  $L_p$  and  $S_p$  are the total orbital and spin angular momenta of the electronic shell, respectively, the  $\chi_p$  denote other quantum numbers needed to identify the basis configurations, and the  $\alpha_p^n$  are the mixing coefficients.

For bound-continuum transitions, the initial states for each R-matrix run are identical to the intermediate excited states (13) described above. To obtain the final ionic states of Ne<sup>+</sup>, we first individually optimized each of the configurations from the following lists:

- (a) Odd parity:  $1s^22s^22p^5$ ,  $1s^22s^22p^43p$ ,  $1s^22s^22p^33s^2$ ,  $1s^22s^22p^34s^2$ ,  $1s^22s^22p^33p^2$ ,  $1s^22s^22p^33d^2$ ,  $1s^22s^12p^53s$ ,  $1s^22s^12p^53d$ ,  $1s^22s^12p^54s$ ,  $1s^22s^02p^53s^2$ ,  $1s^22s^02p^53d^2$ ,  $1s^22s^02p^54s^2$ ,  $1s^22s^02p^53p^2$ .
- (b) Even parity:  $1s^22s^12p^6$ ,  $1s^22s^12p^53p$ ,  $1s^22s^12p^43s^2$ ,  $1s^22s^12p^44s^2$ ,  $1s^22s^12p^43d^2$ ,  $1s^22s^12p^43p^2$ ,  $1s^22s^22p^43s$ ,  $1s^22s^22p^43d$ ,  $1s^22s^22p^44s$ ,  $1s^22s^02p^63s$ ,  $1s^22s^02p^63d$ ,  $1s^22s^02p^64s$ .

All possible *LS* terms were constructed. Then, similarly to the intermediate excited states, the Breit-Pauli Hamiltonian was diagonalized in the basis of the above configurations for



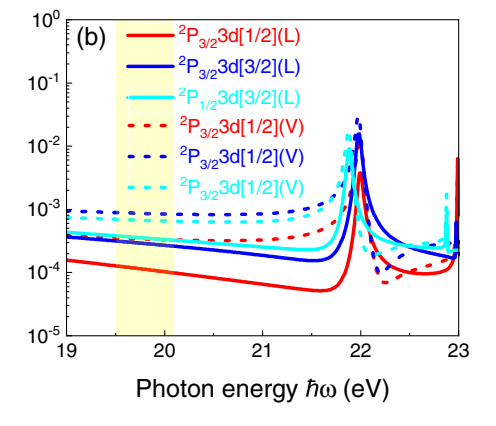


FIG. 4. Photoionization cross section obtained in the length (solid line) and velocity gauge (dashed lines) of polarized 4s and 4s' (a) and 3d (b) states by linearly polarized fields. The shaded (yellow) region indicates the range of photon energies used in the experiment.

TABLE I. *Ab initio* results for helium using the time-dependent close-coupling method. The peak intensity of the fundamental  $\omega$  is  $I_1 = 10^{13}$  W/cm<sup>2</sup>, and the intensity of the second harmonic  $2\omega$  is  $I_2 = 2 \times 10^{12}$  W/cm<sup>2</sup>. Both pulse durations (FWHM) are 7 fs.

$\hbar\omega$ (eV)	$c_s \times 10^3$	$c_p \times 10^2$	$c_d \times 10^3$	$\delta_{sd}$	$\delta_{pd}$	$A_{\omega}^{(h)} \times 10^2$	$\phi_{\omega}^{(h)}$
19.6	-0.97	8.86	-6.62	4.73	1.97	7.5	0.92
19.7	-1.10	8.82	-6.60	4.72	1.96	7.5	0.89
19.75	-1.16	8.80	-6.60	4.72	1.96	7.6	0.88
19.8	-1.23	8.74	-6.59	4.71	1.96	7.7	0.86
19.9	-1.39	8.69	-6.59	4.71	1.96	7.8	0.82
20.0	-1.56	8.61	-6.60	4.70	1.96	8.0	0.78
20.1	-1.75	8.56	-6.62	4.69	1.95	8.2	0.75
20.2	-2.00	8.49	-6.66	4.69	1.95	8.5	0.69

the ionic states with various total angular momentum and parity. The lowest mixed-configuration thresholds with dominating components  $(1s^22s^22p^5)^2P_{3/2;1/2}^o$ ,  $(1s^22s^12p^6)^2S_{1/2}^e$ ,  $(1s^22s^22p^43s)^2S_{1/2}^e$ ,  $^2P_{3/2;1/2}^e$ ,  $^2D_{5/2;3/2}^e$ , and  $^4P_{5/2;3/2;1/2}^e$  were included in the *R*-matrix calculations.

In Fig. 4 we present the photoionization cross sections for magnetic sublevels with projection  $M_J = 0$  of the intermediate 4s and 3d states of neon by a linearly polarized field [Eq. (11) of [36]]. The sharp structures in the photoionization cross sections are due to excitation of the  $2s2p^63s$  autoionizing state (AIS). Even though they are about 2 eV away from the energy range investigated experimentally, the wings may still affect the details of the theoretical predictions. Note the large differences between the results obtained in the length and velocity gauges. Specifically, the peaks just above 22 eV in Fig. 4(a) are only seen in the results obtained in the length gauge, and the peaks seen in Fig. 4(b) at slightly lower photon energies clearly differ in shape, i.e., they are characterized by significantly different Fano q parameters.

This behavior is due to a complex interplay between the initial state, the AIS, and the continuum in which the AIS is embedded. In fact, in simple spectroscopic models, the  $2s2p^63s$  AIS cannot be directly excited from the 3d states. On the other hand, in our extensive R-matrix calculations, the small excitation probability is due to the very small overlap integral  $\langle 3s | 2s \rangle$ . Therefore, even though the dipole matrix

element  $\langle 2p \mid\mid D\mid\mid 3d\rangle$  is quite close in the length and velocity gauges, after multiplying it with  $\langle 3s\mid 2s\rangle$  and summing over all configurations, positive as well as negative values of the matrix element, which determines the sign of the q parameter in the Fano line shape, can be obtained. These observations will be important for the discussion of the agreement between experimental and PT results presented in Sec. IV.

### C. TDSE calculations in helium

The model used for the TDSE calculations in helium is presented elsewhere [23–25]. The helium ionization channels are described by a single quantum number l, corresponding to the orbital momentum of the emitted electron. Indicating each complex ionization amplitude as  $c_l \exp[i\delta_l]$  (l = s, p, d for the three outgoing partial waves), the hemisphere-integrated asymmetry in helium, as a function of the relative phase between the two fields  $\delta = 2\omega\tau$ , is

$$A^{(h)}(\omega,\tau) = \frac{\sqrt{3}c_p[\sqrt{5}c_d\cos(\delta_{pd} + \delta) + 4c_s\cos(\delta_{ps} + \delta)]}{4(c_s^2 + c_p^2 + c_d^2)},$$
(14)

where  $\delta_{ll'} = \delta_l - \delta_{l'}$ .

The values of the magnitudes  $c_l$  and phase difference  $\delta_{ll'}$ , as well as the amplitudes and phases of the asymmetry  $A_{\omega}^{(h)}$  and  $\phi_{\omega}^{(h)}$  for the different photon energies, are shown in Table I. It can be observed that the latter present only a limited variation in the photon energy range of the experiment, as anticipated.

### IV. RESULTS AND DISCUSSION

Figure 5 presents the experimental asymmetries measured in neon and helium in the photon energy range 19.6–20.2 eV. The asymmetries were determined using Eq. (3) and then fitted using the expression given in Eq. (2). The experimental values of the fitting procedure are summarized in Table II.

The small bandwidth  $\Delta\omega$  of the pulses available at FERMI  $(\Delta\omega\simeq 10^{-3}\omega)$  allows one to characterize the influence of the resonance on the asymmetric photoemission. In neon (see Fig. 5), the amplitudes of the oscillation and the phase strongly depend on the photon energy, while the measurements in helium exhibit only a small variation of the amplitude

TABLE II. Photon energies  $\hbar\omega$ , amplitudes  $(A_{\omega}^{(k)})$ , and phases  $(\phi_{\omega}^{(k)})$  of the asymmetry oscillations for neon and helium obtained from Eq. (2) for the experimental data presented in Fig. 5, together with the relative amplitude  $A_{\omega}$  and phase  $\phi_{\omega}$ . The uncertainty in the photon energy was estimated based on the typical bandwidth of the pulses generated at FERMI [27], while the uncertainties for the amplitudes and phases were extracted from the sinusoidal fits shown in Fig. 5.

Photon energy	Neon		Helium		Rel. amplitude	Rel. phase	
$\hbar\omega$ (eV)	$A_{\omega}^{(n)}$ (×100)	$\phi_{\omega}^{(n)}$ (rad)	$A_{\omega}^{(h)}$ (×100)	$\phi_{\omega}^{(h)}$ (rad)	$\overline{A_{\omega} = A_{\omega}^{(n)} / A_{\omega}^{(h)}}$	$\overline{\phi_{\omega} = \phi_{\omega}^{(n)} - \phi_{\omega}^{(h)} \text{ (rad)}}$	
$19.60 \pm 0.02$	$1.3 \pm 0.8$	$0.63 \pm 0.59$	$1.6 \pm 0.3$	$1.02 \pm 0.19$	$0.8 \pm 0.5$	$-0.39 \pm 0.62$	
$19.70 \pm 0.02$	$2.6 \pm 0.4$	$1.09 \pm 0.17$	$2.7 \pm 0.3$	$0.24 \pm 0.13$	$1.0 \pm 0.2$	$0.85 \pm 0.21$	
$19.75 \pm 0.02$	$1.9 \pm 0.4$	$0.31 \pm 0.24$	$1.3 \pm 0.2$	$0.30 \pm 0.17$	$1.5 \pm 0.4$	$0.01 \pm 0.29$	
$19.80 \pm 0.02$	$3.5 \pm 0.5$	$1.84 \pm 0.14$	$1.7 \pm 0.4$	$0.98 \pm 0.23$	$2.1 \pm 0.6$	$0.86 \pm 0.27$	
$19.90 \pm 0.02$	$1.2 \pm 0.5$	$0.93 \pm 0.42$	$2.4 \pm 0.3$	$0.47 \pm 0.15$	$0.5 \pm 0.2$	$0.45 \pm 0.45$	
$20.00 \pm 0.02$	$1.0 \pm 0.4$	$0.51 \pm 0.49$	$2.6 \pm 0.3$	$1.08 \pm 0.15$	$0.4 \pm 0.2$	$-0.57 \pm 0.51$	
$20.10 \pm 0.02$	$0.2 \pm 0.2$	$2.11 \pm 1.65$	$1.9 \pm 0.4$	$1.12 \pm 0.20$	$0.1 \pm 0.1$	$0.99 \pm 1.66$	
$20.20 \pm 0.02$	$0.3 \pm 0.3$	$1.04 \pm 0.79$	$2.3 \pm 0.4$	$0.93 \pm 0.17$	$0.1 \pm 0.1$	$0.11 \pm 0.81$	

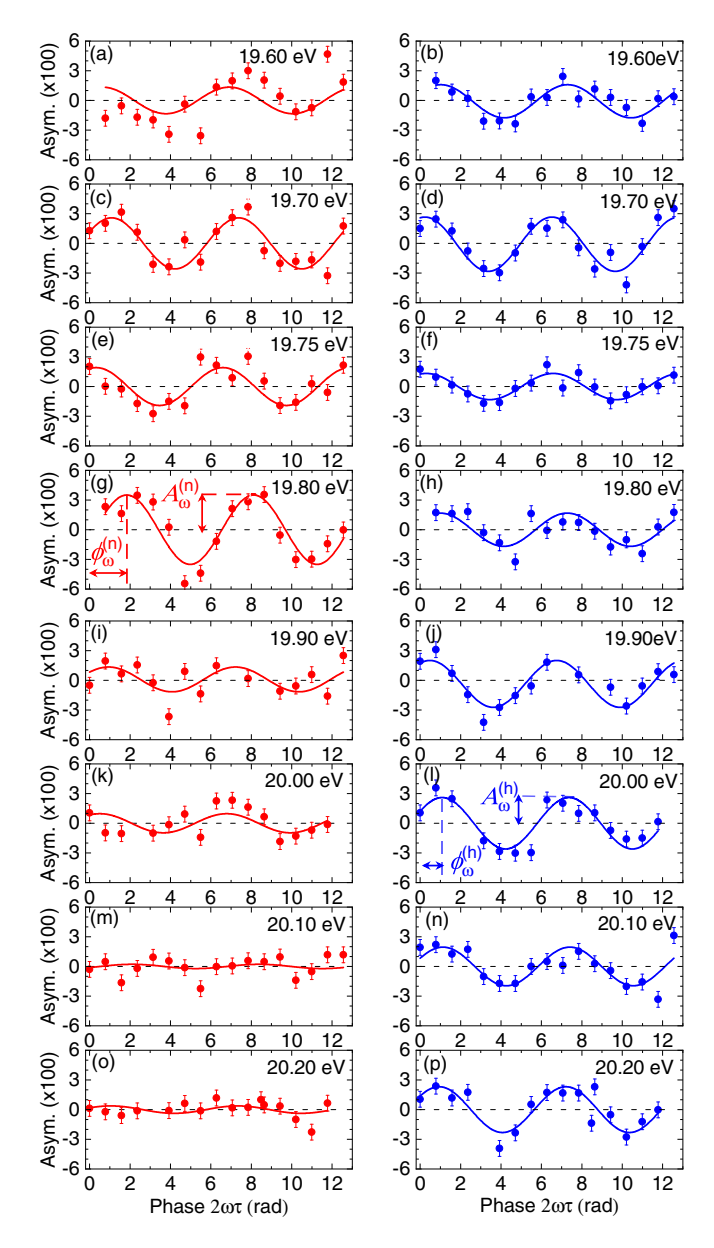


FIG. 5. (a)–(p) Experimental asymmetry (solid circles) as a function of the relative phase  $2\omega\tau$  between the two harmonics measured in neon (a), (c), (e), (g), (i), (k), (m), (o) and helium (b), (d), (f), (h), (j), (l), (n), (p) for the photon energies E=19.6 eV (a), (b), E=19.7 eV (c), (d), E=19.75 eV (e), (f), E=19.8 eV (g), (h), E=19.9 eV (i), (j), E=20.0 eV (k), (l), E=20.1 eV (m),(n), and E=20.2 eV (o), (p). The solid lines represent the sinusoidal fit of the asymmetry curves. The definitions of  $A_{\omega}^{(k)}$  and  $\phi_{\omega}^{(k)}$  [see Eq. (2)] for neon (k=n) and helium (k=h) are shown in panels (g) and (l), respectively.

of the oscillation when changing the photon energy. The quantities measured in helium were used to rescale those measured in neon, introducing the relative amplitude  $A_{\omega} = A_{\omega}^{(n)}/A_{\omega}^{(h)}$  and relative phase  $\phi_{\omega} = \phi_{\omega}^{(n)} - \phi_{\omega}^{(h)}$ . This procedure allows one to isolate the effect of the neon resonance on the variations of the amplitude and phase of the asymmetry and thereby to rule out the contribution of an unaccounted phase shift or a modified harmonic ratio between the two colors. The values of  $A_{\omega}$  and  $\phi_{\omega}$  are also listed in Table II.

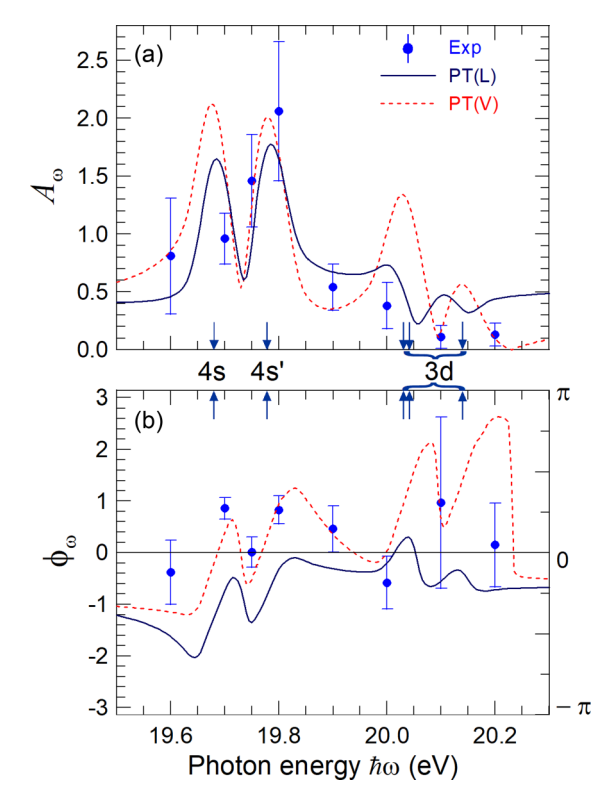


FIG. 6. The relative amplitude ratio  $A_{\omega} = A_{\omega}^{(n)}/A_{\omega}^{(h)}$  (a) and relative phase difference  $\phi_{\omega} = \phi_{\omega}^{(n)} - \phi_{\omega}^{(h)}$  (b) of the hemisphere-integrated asymmetry from Eq. (2) as functions of the photon energy. The positions of the resonance states in neon are indicated on the energy axis. The solid dark-blue and dashed red lines correspond to PT calculations in the length (L) and velocity (V) gauges, respectively, while the blue circles represent the experimental points.

The comparison between the experimental data and the predictions of the PT (carried out for both the length and velocity forms of the electric dipole operator) is presented in Fig. 6. There is reasonable agreement in the energy region around the 4s and 4s' states. The experimental data confirm the decrease of the amplitude of the oscillations for photon energies above ≈19.8 eV predicted by the PT. However, major differences between the experimental and theoretical results appear in the vicinity of the 3d state(s), where the PT in the velocity gauge predicts much larger asymmetries than those observed in the experiment as well as those obtained in the length gauge. The large difference in the visibility of the asymmetry predicted in the two gauges around the 3dresonance can be understood by looking at the photoionization cross section for the intermediate states in the two gauges (cf. Fig. 4).

For the 4s and 4s' states, the predictions calculated in the length and velocity gauges are very close in the photon energy range of the experiment [yellow shaded area in Fig. 4(a)]. As a result, the asymmetries predicted in the two gauges (see Fig. 6) present a similar evolution around the region of these resonances. On the other hand, the photoionization cross sections of the 3d intermediate state exhibit a significant difference between the two gauges, indicating a different coupling between the excited state and the AIS [see yellow shaded area in Fig. 4(b)].

The sensitivity of the results for energies in the 19–20 eV range to the gauge used can be explained by (i) the presence of a Cooper minimum in the  $3d \rightarrow \varepsilon f$  ionization channel, which results in the zero crossing of the corresponding magnitudes to occur at slightly different photon energies in the length- and velocity-gauge calculations, and (ii) the presence of the  $2s2p^63s$  AIS. The latter induces a strong channel interaction, resulting in the ionization cross section of the 3d states predicted in the length gauge to come out one order of magnitude smaller compared to the velocity gauge. For this reason, the amplitude of the asymmetry in the length gauge almost vanishes for photon energies in the 20.0-20.2 eV range [see Fig. 6(a)].

For the phase  $\phi_{\omega}$  presented in Fig. 6(b), the experimental results appear to be in better agreement with the theoretical predictions obtained in the velocity rather than the length gauge. We currently have no explanation for this result. It may just serve as another illustration of the challenges faced in both the measurement and the theoretical description.

### V. CONCLUSION

In conclusion, we have shown how an intermediate atomic resonance affects the amplitudes and phases of the asymmetries observed in a two-color  $\omega-2\omega$  coherent control experiment. The experimental data are in fair agreement with a model based on perturbation theory. Large differences seen between the results obtained in the length and velocity gauges, however, indicate that this is a very challenging problem for theory. We therefore hope that the present work will stimulate further efforts by other groups.

Our findings demonstrate that intermediate energy levels can be used as an additional parameter to control the details of the photoionization process. Such states may open interesting perspectives for the extension of the coherent control technique in the XUV regime to the investigation of molecular resonances, where the presence of rotational, vibrational, and electronic resonances is expected to deliver additional com-

plexity to the problem. In particular, our results are relevant for the development of coherent control schemes using tunable XUV and x-ray pulses in the proximity of resonances embedded in the continuum (as, for example, in x-ray absorption near-edge structure spectroscopy) down to the attosecond domain [37].

### ACKNOWLEDGMENTS

N.D. and K.B. acknowledge funding from the United States National Science Foundation through Grants No. PHY-2012078, No. PHY-1803844, and No. PHY-2110023, respectively, as well as the XSEDE supercomputer allocation No. PHY-090031. K.U. acknowledges support by the X-ray Free Electron Laser Utilization Research project and the X-ray Free Electron Laser Priority Strategy Program of the Ministry of Education, Culture, Sports, Science, and Technology of Japan (MEXT), by the IMRAM program of Tohoku University, and by the Dynamic Alliance for Open Innovation Bridging Human, Environment and Materials program. K.L.I. gratefully acknowledges support by the Cooperative Research Program of the Network Joint Research Center for Materials and Devices (Japan), the Dynamic Alliance for Open Innovation Bridging Human, Environment and Materials Program (Japan), JSPS KAKENHI Grant No. JP19H00869, JST CREST Grant No. JPMJCR15N1, and JST COI Grant No. JPMJCE1313. V.W. acknowledges funding from the Fonds de recherche du Québec-Nature et technologies (FRONT) and the National Science and Engineering Research Council (NSERC). M.M. acknowledges support by the Deutsche Forschungsgemeinschaft (DFG, German Research Foundation)-SFB-925-Project No. 170620586. F.S. acknowledges support by the Deutsche Forschungsgemeinschaft (DFG, German Research Foundation) project STI 125/19-2. G.S. acknowledges financial support by the Deutsche Forschungsgemeinschaft Grant No. 429805582 (Project SA 3470/4-1). We acknowledge support by the Open Access Publication Fund of the University of Freiburg.

<sup>[1]</sup> M. Shapiro and P. Brumer, Laser control of product quantum state populations in unimolecular reactions, J. Chem. Phys. **84**, 4103 (1986).

<sup>[2]</sup> R. J. Levis and H. A. Rabitz, Closing the loop on bond selective chemistry using tailored strong field laser pulses, J. Phys. Chem. A 106, 6427 (2002).

<sup>[3]</sup> M. Dantus and V. V. Lozovoy, Experimental coherent laser control of physicochemical processes, Chem. Rev. 104, 1813 (2004).

<sup>[4]</sup> V. I. Prokhorenko, A. M. Nagy, S. A. Waschuk, L. S. Brown, R. R. Birge, and R. J. D. Miller, Coherent control of retinal isomerization in bacteriorhodopsin, Science 313, 1257 (2006).

<sup>[5]</sup> M. J. Wright, S. D. Gensemer, J. Vala, R. Kosloff, and P. L. Gould, Control of Ultracold Collisions with Frequency-Chirped Light, Phys. Rev. Lett. 95, 063001 (2005).

<sup>[6]</sup> J. J. García-Ripoll, P. Zoller, and J. I. Cirac, Speed Optimized Two-Qubit Gates with Laser Coherent Control Techniques for

Ion Trap Quantum Computing, Phys. Rev. Lett. **91**, 157901 (2003).

<sup>[7]</sup> L. Giannessi, E. Allaria, K. C. Prince, C. Callegari, G. Sansone, K. Ueda, T. Morishita, C. N. Liu, A. N. Grum-Grzhimailo, E. V. Gryzlova *et al.*, Coherent control schemes for the photoionization of neon and helium in the Extreme Ultraviolet spectral region, Sci. Rep. 8, 7774 (2018).

<sup>[8]</sup> A. M. Weiner, Femtosecond pulse shaping using spatial light modulators, Rev. Sci. Instrum. 71, 1929 (2000).

<sup>[9]</sup> K. Bergmann, H. Theuer, and B. W. Shore, Coherent population transfer among quantum states of atoms and molecules, Rev. Mod. Phys. **70**, 1003 (1998).

<sup>[10]</sup> N. B. Baranova, I. M. Beterov, B. Y. Zel'dovich, I. I. Ryabtsev, A. N. Chudinov, and A. A. Shul'ginov, Observation of an interference of one- and two-photon ionization of the sodium 4s state, Pis'ma Zh. Eksp. Teor. Fiz. 55, 431 (1992) [JETP Lett. 55, 439 (1992)].

- [11] R. Yamazaki and D. S. Elliott, Observation of the Phase Lag in the Asymmetric Photoelectron Angular Distributions of Atomic Barium, Phys. Rev. Lett. **98**, 053001 (2007).
- [12] R. Yamazaki and D. S. Elliott, Strong variation of the phase lag in the vicinity of autoionizing resonances, Phys. Rev. A 76, 053401 (2007).
- [13] A. N. Grum-Grzhimailo, E. V. Gryzlova, E. I. Staroselskaya, J. Venzke, and K. Bartschat, Interfering one-photon and twophoton ionization by femtosecond VUV pulses in the region of an intermediate resonance, Phys. Rev. A 91, 063418 (2015).
- [14] N. Douguet, A. N. Grum-Grzhimailo, E. V. Gryzlova, E. I. Staroselskaya, J. Venzke, and K. Bartschat, Photoelectron angular distributions in bichromatic atomic ionization induced by circularly polarized VUV femtosecond pulses, Phys. Rev. A 93, 033402 (2016).
- [15] N. Douguet, E. V. Gryzlova, E. I. Staroselskaya, K. Bartschat, and A. N. Grum-Grzhimailo, Photoelectron angular distribution in two-pathway ionization of neon with femtosecond XUV pulses, Eur. Phys. J. D 71, 105 (2017).
- [16] E. Allaria, R. Appio, L. Badano, W. A. Barletta, S. Bassanese, S. G. Biedron, A. Borga, E. Busetto, D. Castronovo, P. Cinquegrana *et al.*, Highly coherent and stable pulses from the FERMI seeded free-electron laser in the extreme ultraviolet, Nat. Photon. 6, 699 (2012).
- [17] K. C. Prince, E. Allaria, C. Callegari, R. Cucini, G. D. Ninno, S. D. Mitri, B. Diviacco, E. Ferrari, P. Finetti, D. Gauthier *et al.*, Coherent control with a short-wavelength free-electron laser, Nat. Photon. 10, 176 (2016).
- [18] P. K. Maroju, C. Grazioli, M. Di Fraia, M. Moioli, D. Ertel, H. Ahmadi, O. Plekan, P. Finetti, E. Allaria, L. Giannessi et al., Attosecond pulse shaping using a seeded free-electron laser, Nature (London) 578, 386 (2020).
- [19] P. K. Maroju, C. Grazioli, M. D. Fraia, M. Moioli, D. Ertel, H. Ahmadi, O. Plekan, P. Finetti, E. Allaria, L. Giannessi *et al.*, Analysis of two-color photoelectron spectroscopy for attosecond metrology at seeded free-electron lasers, New J. Phys. 23, 043046 (2021).
- [20] P. K. Maroju, C. Grazioli, M. D. Fraia, M. Moioli, D. Ertel, H. Ahmadi, O. Plekan, P. Finetti, E. Allaria, L. Giannessi *et al.*, Complex attosecond waveform synthesis at FEL FERMI, Appl. Sci. 11, 9791 (2021).
- [21] V. Lyamayev, Y. Ovcharenko, R. Katzy, M. Devetta, L. Bruder, A. LaForge, M. Mudrich, U. Person, F. Stienkemeier, M. Krikunova *et al.*, A modular end-station for atomic, molecular, and cluster science at the low density matter beamline of FERMI@Elettra, J. Phys. B: At. Mol. Opt. Phys. 46, 164007 (2013).
- [22] L. A. A. Nikolopoulos and P. Lambropoulos, Multichannel theory of two-photon single and double ionization of helium, J. Phys. B: At. Mol. Opt. Phys. 34, 545 (2001).
- [23] K. L. Ishikawa and K. Midorikawa, Above-threshold double ionization of helium with attosecond intense soft x-ray pulses, Phys. Rev. A **72**, 013407 (2005).

- [24] K. L. Ishikawa and K. Ueda, Competition of Resonant and Nonresonant Paths in Resonance-Enhanced Two-Photon Single Ionization of He by an Ultrashort Extreme-Ultraviolet Pulse, Phys. Rev. Lett. 108, 033003 (2012).
- [25] K. L. Ishikawa and K. Ueda, Photoelectron angular distribution and phase in two-photon single ionization of H and He by a femtosecond and attosecond extreme-ultraviolet pulse, Appl. Sci. 3, 189 (2013).
- [26] C. Svetina, C. Grazioli, N. Mahne, L. Raimondi, C. Fava, M. Zangrando, S. Gerusina, M. Alagia, L. Avaldi, G. Cautero et al., The low density matter (LDM) beamline at FERMI: Optical layout and first commissioning, J. Synchrotron Radiat. 22, 538 (2015).
- [27] P. Finetti, H. Höppner, E. Allaria, C. Callegari, F. Capotondi, P. Cinquegrana, M. Coreno, R. Cucini, M. B. Danailov, A. Demidovich *et al.*, Pulse Duration of Seeded Free-Electron Lasers, Phys. Rev. X 7, 021043 (2017).
- [28] B. Diviacco, R. Bracco, D. Millo, and M. Musardo, IPAC 2011—2nd International Particle Accelerator Conference, 3278 (2011).
- [29] C. J. Dasch, One-dimensional tomography: A comparison of Abel, onion-peeling, and filtered backprojection methods, Appl. Opt. 31, 1146 (1992).
- [30] S. Manzhos and H.-P. Loock, Photofragment image analysis using the onion-peeling algorithm, Comput. Phys. Commun. 154, 76 (2003).
- [31] M. J. J. Vrakking, An iterative procedure for the inversion of two-dimensional ion/photoelectron imaging experiments, Rev. Sci. Instrum. 72, 4084 (2001).
- [32] E. V. Gryzlova, A. N. Grum-Grzhimailo, E. I. Staroselskaya, N. Douguet, and K. Bartschat, Quantum coherent control of the photoelectron angular distribution in bichromatic-field ionization of atomic neon, Phys. Rev. A 97, 013420 (2018).
- [33] E. V. Gryzlova, M. M. Popova, A. N. Grum-Grzhimailo, E. I. Staroselskaya, N. Douguet, and K. Bartschat, Coherent control of the photoelectron angular distribution in ionization of neon by a circularly polarized bichromatic field in the resonance region, Phys. Rev. A 100, 063417 (2019).
- [34] T. Pauly, A. Bondy, K. R. Hamilton, N. Douguet, X.-M. Tong, D. Chetty, and K. Bartschat, Ellipticity dependence of excitation and ionization of argon atoms by short-pulse infrared radiation, Phys. Rev. A 102, 013116 (2020).
- [35] O. Zatsarinny, BSR: *B*-spline atomic *R*-matrix codes, Comput. Phys. Commun. **174**, 273 (2006).
- [36] E. V. Gryzlova, P. O'Keeffe, D. Cubaynes, G. A. Garcia, L. Nahon, A. N. Grum-Grzhimailo, and M. Meyer, Isotope effects in resonant two-color photoionization of Xe in the region of the  $5P^5(^2P_{1/2})4f[5/2]_2$  autoionizing state, New J. Phys. **17**, 043054 (2015).
- [37] S. Mukamel, D. Healion, Y. Zhang, and J. D. Biggs, Multidimensional attosecond resonant x-ray spectroscopy of molecules: Lessons from the optical regime, Annu. Rev. Phys. Chem. **64**, 101 (2013).